

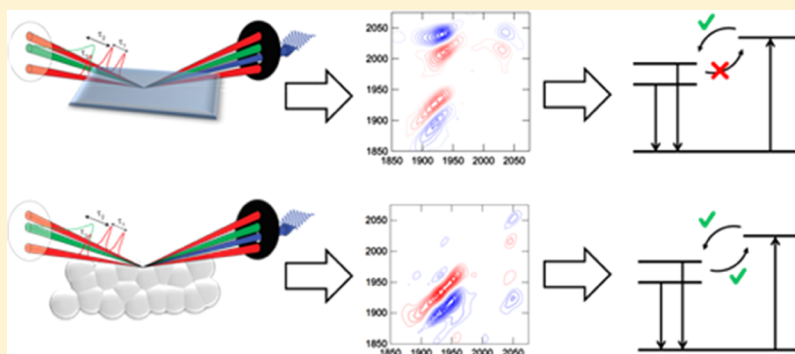
Distinct Binding of Rhenium Catalysts on Nanostructured and Single-Crystalline TiO₂ Surfaces Revealed by Two-Dimensional Sum Frequency Generation Spectroscopy

Heather Vanselow,^{†,§} Pablo E. Videla,^{‡,§} Victor S. Batista,^{*,‡,§} and Poul B. Petersen^{*,†,§}

[†]Department of Chemistry and Chemical Biology, Cornell University, Ithaca, New York 14853, United States

[‡]Department of Chemistry and Energy Sciences Institute, Yale University, 225 Prospect Street, New Haven, Connecticut 06520, United States

Supporting Information



ABSTRACT: High surface area TiO₂ electrodes are extensively used in photocatalytic solar cells. However, it remains controversial how molecular catalysts interact with the TiO₂ surfaces and how the electrodes affect the functionality of catalytic adsorbates. Here, we examine the CO₂ reduction catalyst Re^I(dcbpy)(CO)₃Cl (dcbpy = 4,4'-dicarboxy-2,2'-bipyridine) on TiO₂ by probing spectroscopically isolated carbonyl modes that are highly sensitive to the complex electronic structure and solvation environment. Combining interferometric two-dimensional sum frequency generation spectroscopy and *ab initio* simulations of the spectra, we find distinct spectroscopic and dynamical properties of catalysts bound to single crystals and nanocrystalline surfaces. Different cross-peak patterns resulting from interferences between elements of the fourth-order susceptibility, along with different vibrational relaxation dynamics, reveal distinct vibrational relaxation pathways of the catalysts on different TiO₂ surfaces that could be engineered for selective catalytic performance.

INTRODUCTION

Understanding the interactions of catalytic adsorbates at interfaces is essential for a wide range of emerging technologies, including the development of photocatalytic solar cells for water oxidation^{1–6} and revolutionary methods for CO₂ reduction.^{7–11} High surface area titanium dioxide (TiO₂) materials have attracted great interest in photocatalysis and electrocatalysis applications both as photosensitizers (e.g., in photodegradation of organic compounds and water splitting¹²) and sacrificial electron acceptor surfaces (e.g., in dye-sensitized solar cells¹³ and CO₂ photocatalysis¹⁴). However, the efficiency of the catalysts and the reaction pathways are often affected by rearrangements and specific interactions of the molecular adsorbates at TiO₂ interfaces.^{14–29} Sometimes, the surfaces enhance catalytic performance because of favorable adsorbate–surface interactions and efficient charge separation,²⁴ although unfavorable interactions with the surface could be detrimental for catalytic performance. Differences in the binding geometry of molecular catalysts at different surfaces¹⁶ can also increase the number of active sites

per unit area, although the net effect on catalytic performance often remains controversial.^{26–28} Understanding how catalytic adsorbates interact with different metal oxide surfaces at the molecular level is thus essential for the design of efficient catalytic materials such as thin films, nanorods, and nanosheets with high surface area.^{30–38}

Rhenium (Re) tricarbonyl complexes are prototypical model complexes that exhibit both electrocatalytic and photocatalytic activity for reduction of CO₂ to CO.^{39–42} In recent years, Re catalysts have attracted increasing interest.^{9,43} Studies based on vibrational spectroscopy have exploited the CO stretching modes because they provide a highly sensitive probe of the electronic structure and solvation environment.⁴⁴ Transient infrared spectroscopy and two-dimensional infrared (2D IR) spectroscopy have been used to study the ground- and excited-state dynamics of Re complexes in solution^{44–49} as well as

Received: August 29, 2018

Revised: October 22, 2018

Published: October 23, 2018



interfacial electron-transfer dynamics between Re catalysts and TiO_2 thin films.^{29,50} Vibrational sum frequency generation (SFG) spectroscopy has been applied to determine the average molecular orientation of Re catalysts at interfaces.^{51–54} Time-resolved SFG spectroscopy has probed the ultrafast vibrational dynamics of Re complexes on solid surfaces.^{55–58} An outstanding challenge is to characterize the distinct arrangement of adsorbates at the molecular level, using spectroscopic techniques with both high frequency and high temporal resolution, as needed to resolve the vibronic couplings and ultrafast relaxation dynamics.

2D vibrational spectroscopy, including 2D IR and 2D SFG spectroscopy,^{59,60} offers both high spectral and temporal resolution. By spreading the molecular response into two frequency dimensions, these techniques resolve the couplings and correlations between different vibrational modes.⁸¹ Moreover, the high temporal resolution provides dynamical information on the subpicosecond timescale and allows us to elucidate the molecular origin of vibrational relaxation dynamics.⁵⁹ Recent improvements in sensitivity have enabled third-order 2D IR^{59,60} and 2D attenuated total reflectance (ATR) IR^{62–66} studies to probe molecular species interacting with surfaces,^{67–69} although the spectra usually include significant contributions from the bulk solution.

2D SFG spectroscopy offers significant advantages over 2D IR because it is a surface-specific technique.⁷⁰ The 2D SFG signal results from a fourth-order response that averages to zero for molecules randomly oriented in the isotropic bulk media.⁷¹ Besides characterization of vibrational frequencies, 2D SFG provides information on homogeneous and heterogeneous broadening as well as vibrational couplings often sensitive to the molecular order and orientation at the interface, making it an ideal tool to study adsorbate–interface interactions. Detailed characterization of the orientation of molecular adsorbates at interfaces can reveal fundamental aspects of vibrational dynamics and characterization of ultrafast relaxation processes.^{72,73}

We combine the recently developed interferometric 2D SFG spectroscopy^{70,72,73} and calculations based on density functional theory (DFT) to examine the distinct binding of Re catalysts on single-crystalline and nanostructured TiO_2 surfaces. We resolve the femtosecond vibrational relaxation dynamics with both high frequency and high temporal resolution. Long acquisition times are enabled by the high stability of data collection achieved by interferometric 2D SFG experiments.^{73–75} Distinct interactions between the catalyst and various TiO_2 surfaces are probed and characterized through changes in the carbonyl vibrational bands of the Re tricarbonyl catalyst bound to single-crystal rutile (110), rutile (001), and anatase (101) surfaces. The spectra reveal different vibrational couplings and relaxation timescales for different TiO_2 surfaces, consistent with distinct molecular orientations and arrangements of molecular adsorbates at TiO_2 interfaces.

EXPERIMENTAL SECTION

Sample Preparation. $\text{Re}(4,4'\text{-dicarboxyl-2,2'}\text{-bipyridine})\text{-(CO)}_3\text{Cl}$, abbreviated as $\text{Re}(\text{CO})_3$ throughout this paper (see Figure 1), was synthesized according to published procedures.^{40,75} Polished single-crystal rutile (110) and (001) substrates were purchased from MTI Corporation, and anatase (101) was purchased from SurfaceNet GmbH. The substrates were pretreated⁷⁶ in basic piranha solution (1:1:2 $\text{H}_2\text{O}_2/\text{NH}_4\text{OH}/\text{H}_2\text{O}$) at 80 °C for 10 min and rinsed thoroughly

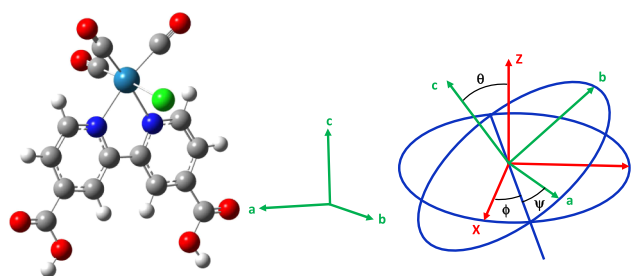


Figure 1. Left: Optimized DFT structure of the $\text{Re}(\text{CO})_3$ complex and definition of the molecular frame (a , b , c axis). The a – c plane is defined as the plane of the bipyridine ring. The atoms are colored as follows: green, Cl; white, H; red, O; gray, C; blue, N; and cyan, Re. Right: Schematic illustration of the orientation angles used to model the complex's orientation. Axis X , Y , and Z represent the laboratory frame and θ , ϕ , and ψ are the Euler angles.

with ultrapure water (Millipore Milli-Q, 18.2 $\text{M}\Omega\text{-cm}$, ≤ 5 ppb total organic carbon) until neutral pH was achieved. The crystals were sensitized overnight in $\text{Re}(\text{CO})_3$ -saturated ethanol solution, rinsed with excess ethanol, and dried before use.

HD and 2D SFG Experiments. The experimental details for the heterodyne (HD)-detected⁷³ and 2D SFG⁷⁴ have been previously described. Briefly, a Ti:sapphire oscillator (Coherent Micra-5) seeded a Ti:sapphire amplifier (Coherent Legend Elite Duo), which produced 800 nm pulses (5 mJ, 25 fs, 1 kHz). The 800 nm beam was split into three separate beams. One beam contained 0.75 mJ and was spectrally narrowed using Fabry–Perot etalon (TecOptics, Inc.) to create the visible upconversion pulse [792.3, 0.7 nm full width at half-maximum (fwhm)]. Another beam contained 3 mJ and was used to pump a commercial optical parametric amplifier (Coherent OPerA Solo), which generated tunable mid-IR pulses (1924, 249 cm^{-1} fwhm). The IR pulses were split into a probe pulse and a pump pulse with a KBr beamsplitter. The pump was further split, interfered in a Mach–Zehnder interferometer, and recombined collinearly. An external local oscillator (LO) was generated spatially before the sample in transmission by focusing the visible and IR beams in a ZnO -coated (150 nm) 0.7 mm thick CaF_2 window. The three beams (visible, IR probe, and SFG_{LO}) were recollimated with an off-axis parabolic mirror. A delay plate, 2 mm thick SiO_2 , was used to temporally delay the SFG_{LO} beam. The visible (10.4 μJ), IR probe (3.5 μJ), and IR pump pair (2.6 μJ in each arm) were focused on the sample with another off-axis parabolic mirror at 60°, 65°, and 55° with respect to the surface normal in the ppppp polarization combination (polarization of SFG, visible, IR probe, and each IR pump pulse, respectively). The emitted SFG signal was dispersed by a grating and imaged onto a liquid nitrogen-cooled charge-coupled device (CCD) (Princeton Instruments, model 7509-0001, 1340 \times 400 pixels). To correct for potential laser fluctuations and sample degradation, the pump was synchronized with an optical chopper which was triggered by the laser (every other pump pulse in one arm of the interferometer was blocked by the chopper). A galvanometric mirror was fed a 500 Hz sine wave and also synchronized with the laser, and it spatially separated the generated SFG field influenced by one pump from the SFG field with two interfering pumps on the CCD.⁷⁷

An interferogram was formed in the pump axis, τ_1 , by scanning one pump with respect to the other with a step size of

2 fs from −100 to 1500 fs. At each time, HD-detected SFG data were collected in the probe axis with an integration time of 5 s. The HD SFG signal was collected as a function of τ_1 , and the signal was Fourier-transformed to obtain a complex signal which was a function of two frequency variables, ω_1 and ω_3 . The zero timing of the τ_1 delay was set by the IR–IR autocorrelation. The phase of the ω_3 axis was set by dividing the sample response with the nonresonant response from gold and requiring the imaginary component of the nonlinear susceptibility to be zero far from the resonances, as previously described for HD SFG.⁷³

For each sample, the data were averaged over four 2D acquisitions, with the exception of anatase (101) which was an average of two. A series of waiting times, τ_2 , were collected by delaying the visible and IR probe pulses with respect to the stationary pump. The frequency resolution in the probe axis was 10 cm^{−1} as set by the visible upconversion pulse. The frequency resolution in the pump axis was 22 cm^{−1} as set by the step size and distance scanned between the pump pulses. The temporal resolution in τ_2 was 100 fs, determined by the third-order IR_{pump}–IR_{probe}–visible cross-correlation.

Ab Initio 2D SFG Spectra. The calculation of DFT 2D SFG spectra is based upon our previous work on simulations of one-dimensional (1D) SFG^{7,53,54,78} and involves the determination of the fourth-order molecular hyperpolarizabilities $\beta_{ijklm}^{(4)}$ based on the following equation

$$\beta_{ijklm}^{(4)} \propto \frac{\partial \alpha_{ij}}{\partial Q_{q_1}} \cdot \frac{\partial \mu_k}{\partial Q_{q_2}} \cdot \frac{\partial \mu_l}{\partial Q_{q_3}} \cdot \frac{\partial \mu_m}{\partial Q_{q_4}} \quad (1)$$

where α_{ij} and μ_k (with $i, j, k = a, b, c$) are elements of the polarizability and dipole moment, respectively, in the molecular frame (see Figure 1) and Q_q is the coordinate of the q -th vibrational normal mode. The subscripts q of Q_q in eq 1 correspond to either the same or different vibrational mode depending on the specific excitation pathway⁷¹ (see Supporting Information). Dipole moments and polarizabilities between the ground and first excited states are obtained by DFT calculations. We employ the harmonic approximation to obtain the transition parameters between the first and second excited states, that is, the ground to first excited state transition parameters are multiplied by $\sqrt{2}$. All DFT calculations were performed using the Gaussian 09, Revision D.01, software package,⁷⁹ with the B3LYP hybrid functional⁸⁰ and the SDD basis sets⁸¹ for Re and the 6-311+G(d) basis set for all nonmetal atoms. We employed the “tight” optimization criteria and ultrafine grid integration. The use of a different basis set for Re such as LANL2DZ⁸² or CEP-121G⁸³ does not substantially change the transition dipole moments or polarizabilities. Therefore, we only show results for the SDD basis set.

The molecular response (eq 1) is rotated to the laboratory frame to obtain the fourth-order susceptibility, defined as follows

$$\chi_{IJKLM}^{(4)} = \sum_{ijklm} \langle R_{Ii} \cdot R_{Jj} \cdot R_{Kk} \cdot R_{Ll} \cdot R_{Mm} \rangle \cdot \beta_{ijklm}^{(4)} \quad (2)$$

where R_{ij} represents elements of the (ZZZ) Euler rotation matrix that connect the molecular coordinate frame (with $i, j, k, l, m = a, b, c$) to the laboratory coordinate frame (with $I, J, K, L, M = X, Y, Z$) through the Euler angles θ , ψ , and ϕ (see Figure 1).⁸⁴ The angle brackets in eq 2 represent rotational

averages over the molecular distribution of orientations. Two different distributions were considered for the azimuthal angle, including a δ -function distribution characterized by a fixed angle ϕ and a uniform distribution over configurations differing in $\Delta\phi$, where $\Delta\phi = 10^\circ, 45^\circ$, or 90° . The angle ψ was set to 0° for all calculations (see Supporting Information) because our previous studies found that the molecule binds in a bidentate mode to crystalline TiO₂ and does not rotate freely along the internal axis.^{7,53,78}

The peak intensity of the 2D SFG spectra is proportional to the effective susceptibility, given by the general form

$$\chi_{\text{eff}} = \sum_{IJKLM} C_I(\omega_{\text{SFG}}) \cdot C_J(\omega_{\text{vis}}) \cdot C_K(\omega_{\text{IR},3}) \cdot C_L(\omega_{\text{IR},2}) \cdot C_M(\omega_{\text{IR},1}) \chi_{IJKLM}^{(4)} \quad (3)$$

where $C(\omega)$ are prefactors that depend on the beam incident angles, frequency, and light polarization. For all-p-polarized light, they take the form^{71,84}

$$\begin{aligned} C_X(\omega) &= L_{XX}(\omega) \cos(\gamma) \\ C_Y(\omega) &= 0 \\ C_Z(\omega) &= L_{ZZ}(\omega) \sin(\gamma) \end{aligned} \quad (4)$$

where L are Fresnel factors of the interface and γ is the incident angle of the light pulse. We use the experimental incident beam angles ($\gamma_{\text{IR},1} = \gamma_{\text{IR},2} = 55^\circ$, $\gamma_{\text{IR},3} = 65^\circ$, $\gamma_{\text{vis}} = 60^\circ$) and calculated the Fresnel factors^{85,86} using $n_{\text{air}} = 1$, $n_{\text{TiO}_2} = 2.52$,^{87,88} and $n_{\text{interf}} = 1.62$.⁸⁶ The final values of the prefactors C introduced by eq 4 are listed in Table S1.

The final line shapes of the ab initio 2D SFG spectra were modeled by computing the pure absorptive spectra given by

$$\begin{aligned} R(\omega_1, \omega_3) &= \int_{-\infty}^{\infty} dt_1 e^{i\omega_1 t_1} \int_{-\infty}^{\infty} dt_3 [e^{i\omega_3 t_3} R_{\text{R}}(t_1, t_3) \\ &\quad + e^{-i\omega_3 t_3} R_{\text{NR}}(t_1, t_3)] \end{aligned} \quad (5)$$

where R_{R} and R_{NR} are the rephasing and nonrephasing responses, respectively. The 2D vibrational responses were modeled using Bloch dynamics,⁵⁹ in which the rephasing response is given by

$$R_{\text{R}}(t_1, t_3) = \sum_{i=1}^3 R_i(t_1, t_3) e^{-(t_3+t_1)/T_2} e^{-\delta\Omega^2(t_3-t_1)^2/2} \quad (6)$$

and the nonrephasing response is given by

$$R_{\text{NR}}(t_1, t_3) = \sum_{i=4}^6 R_i(t_1, t_3) e^{-(t_3+t_1)/T_2} e^{-\delta\Omega^2(t_3+t_1)^2/2} \quad (7)$$

where T_2 and $\delta\Omega$ are the homogeneous and inhomogeneous broadening parameters, respectively. In this paper, we set $T_2 = 1$ ps and $\delta\Omega = 1$ ps^{−1}. In the previous equations, R_i represents one of the six generic excitation pathways for 2D SFG, shown in Figure S1⁵⁹

$$R_1(t_1, t_3) = i \sum_{p,q} \chi_{\text{eff}}^{(4)} e^{i(\omega_q t_1 - \omega_p t_3)} \quad (8)$$

$$R_2(t_1, t_3) = i \sum_{p,q} \chi_{\text{eff}}^{(4)} e^{i(\omega_q t_1 - \omega_p t_3)} \quad (9)$$

$$R_3(t_1, t_3) = -i \sum_{q,r} \chi_{\text{eff}}^{(4)} e^{i(\omega_q t_1 - (\omega_r - \omega_q) t_3)} \quad (10)$$

$$R_4(t_1, t_3) = i \sum_{p,q} \chi_{\text{eff}}^{(4)} e^{i(-\omega_q t_1 - \omega_q t_3)} \quad (11)$$

$$R_5(t_1, t_3) = i \sum_{p,q} \chi_{\text{eff}}^{(4)} e^{i(-\omega_q t_1 - \omega_p t_3)} \quad (12)$$

$$R_6(t_1, t_3) = -i \sum_{p,q,r} \chi_{\text{eff}}^{(4)} e^{i(-\omega_q t_1 - (\omega_r - \omega_p) t_3)} \quad (13)$$

where p and q represent fundamental states (i.e., $|100\rangle$, $|010\rangle$, $|001\rangle$) and r represents overtones and combination bands (i.e., $|110\rangle$, $|101\rangle$, $|011\rangle$, $|200\rangle$, $|020\rangle$, $|002\rangle$). The frequency positions ω were obtained from DFT gas-phase anharmonic calculations of the $\text{Re}(\text{CO})_3$ complex, using vibrational second-order perturbation theory VPT2^{89,90} as implemented in Gaussian 09⁷⁹ ("freq = anharmonic" keyword). All simulated spectra are normalized to the most intense peak and plotted with contour steps of 0.1 from -1 to $+1$. Waiting time τ_2 was set to zero for all DFT spectra.

RESULTS AND DISCUSSION

Fourier Transform IR Spectra. Figure 2 shows the Fourier transform infrared (FTIR) spectrum of the $\text{Re}(\text{dcbpy})\text{-Re}(\text{CO})_3$ complex.

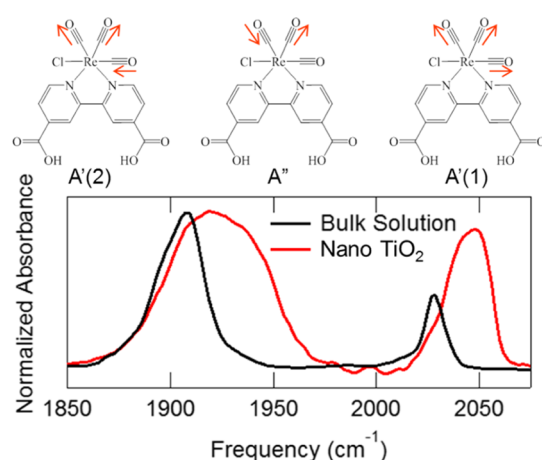


Figure 2. Top: CO vibrational normal modes of $\text{Re}(\text{CO})_3$. Bottom: FTIR spectra of $\text{Re}(\text{CO})_3$ in bulk ethanol solution (black) or immobilized on nanocrystalline TiO_2 nanoparticles (red). The lower frequency band (1910 cm^{-1}) involves the $A'(2)$ and A'' modes, whereas the higher frequency band (2025 cm^{-1}) is due to the $A'(1)$ symmetric stretch.

$(\text{CO})_3\text{Cl}$ (dcbpy = 4,4'-dicarboxy-2,2'-bipyridine) complex (abbreviated as $\text{Re}(\text{CO})_3$ throughout this paper) for the spectral region corresponding to the three CO vibrational modes. The bulk FTIR spectrum was collected for a saturated solution of the catalyst in ethanol (Figure 2, black trace), characterized by two main bands. The lower frequency band at $\sim 1910 \text{ cm}^{-1}$ results from a combination of the $A'(2)$ antisymmetric stretch of axial versus equatorial CO ligands and the A'' antisymmetric stretch of the equatorial carbonyl ligands, whereas the higher frequency mode at $\sim 2025 \text{ cm}^{-1}$ results from the $A'(1)$ symmetric stretch involving all three carbonyl ligands. We note that the frequencies of the CO stretching modes are significantly blue-shifted and broadened when $\text{Re}(\text{CO})_3$ is immobilized on TiO_2 nanoparticles (Figure 2, red trace). The spectra show a broad heterogeneous distribution of vibrational frequencies on nanocrystalline TiO_2 ,

suggesting a broad distribution of binding motifs with distinct environments or perhaps different aggregation states which could influence the degree of charge transfer from the catalyst to the TiO_2 .^{68,91,92}

Surface-Sensitive HD-Detected Measurements. We apply HD SFG spectroscopy to investigate the orientation of the $\text{Re}(\text{CO})_3$ catalyst on crystalline and nanostructured TiO_2 surfaces. The overall orientation is important for the reaction mechanism because CO_2 binds to the Re center from solution and therefore must not be sterically hindered. The SFG signal has predominant contributions from the second-order susceptibility, $\chi^{(2)}$, which averages to zero when the catalyst has an isotropic distribution of orientations, as in the bulk media. Accordingly, the technique provides the vibrational spectra of interfacial species with submonolayer sensitivity.⁹³ Moreover, SFG provides complementary information when compared to IR-based methods because the SFG-active modes are both IR- and Raman-active. The conventional (homodyne) SFG signal lacks phase information because it is determined by the squared magnitude of the second-order susceptibility. HD detection using a reference field^{94,95} allows us to recover the phase of the signal and improve the sensitivity of SFG to gain further information on the orientation of molecular probes. The imaginary part of $\chi^{(2)}$ defines the absorptive response that can be directly compared to the FTIR and Raman spectra, whereas the real part defines the dispersive response.

Figure 3 shows the imaginary part of the (HD) SFG spectra of $\text{Re}(\text{CO})_3$ on different crystalline and nanostructure TiO_2

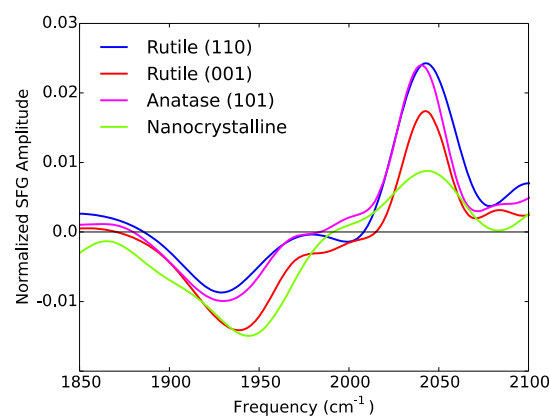


Figure 3. Imaginary component of the HD-detected SFG spectra of $\text{Re}(\text{CO})_3$ on rutile (110) TiO_2 , rutile (001) TiO_2 , anatase (101) TiO_2 , and nanocrystalline TiO_2 surfaces. The spectra are normalized to the total absolute peak area.

surfaces. All spectra have a positive peak at about 2030 cm^{-1} and a negative band at around 1930 cm^{-1} , with the positions of the bands in agreement with FTIR spectra (Figure 2). The sign of the peak with ppp polarization is determined by the projection of the hyperpolarizability tensor along the normal to the surface.⁸⁴ Opposite signs of the high- and low-frequency modes indicate that the transition dipole moments of the symmetric and asymmetric modes are oriented away and toward the surface, respectively.^{7,72,73,78,96} Hence, the molecular orientation is perpendicular to the surface as expected for the complex anchored to TiO_2 through the carboxylate groups, consistent with SFG experiments of analogous $\text{Re}(\text{CO})_3$ monolayers on TiO_2 and gold surfaces.^{7,53,54,73,78}

Although the spectra shown in Figure 3 exhibit opposite signs for the high- and low-frequency modes, the ratio of the

two features is different for different TiO_2 surfaces. The SFG peak intensities are determined by the second-order susceptibility which depends on the orientation of the molecule on the surface.⁸⁴ Hence, different intensity ratios of high- and low-frequency modes reflect differences in molecular orientation. In fact, a larger intensity ratio of the low-to-high frequency modes indicates an orientation farther away from the normal to the surface.⁷⁸ Broader features in the HD SFG spectrum indicate larger heterogeneity, just like in linear FTIR spectra. As seen in Figure 3, the broader distribution corresponds to $\text{Re}(\text{CO})_3$ on nanocrystalline TiO_2 . Therefore, nanocrystalline TiO_2 exhibits the largest heterogeneity. In contrast, all single-crystalline surfaces have roughly the same intensity ratio of asymmetric and symmetric stretch bands, indicating that the catalyst exhibits a narrower range of orientations on crystalline surfaces and is oriented more normal to the surface.^{7,53}

Note that the changes in the intensity ratio between symmetric and asymmetric modes could also be due to changes in the Raman tensor due to interactions with the surface. However, previous studies have suggested that the surface does not exert a significant influence on the transition dipole and polarizability tensors^{53,54,78,92} when $\text{Re}(\text{CO})_3$ is oriented normal to the surface because the carbonyl groups do not have direct contact with TiO_2 in that configuration. We have tested this hypothesis by computing the influence of the TiO_2 surface on the dipole derivatives and polarizability for different orientations of the $\text{Re}(\text{CO})_3$ catalyst (see Section S6 of Supporting Information). The analysis shows that for a wide range of orientations of the complex close to the normal ($|\theta| < \sim 30^\circ$), a range that encloses the most stable orientations of the $\text{Re}(\text{CO})_3$ complex on crystalline TiO_2 surfaces,^{7,53} the influence of the interface on dipole/polarizability derivatives is small. Although we cannot discard the presence of configurations with the catalyst in close contact with the surface for the heterogenous nanocrystalline TiO_2 interface, these results allow us to primarily ascribe the changes in intensity between the symmetric and antisymmetric modes observed in the SFG spectra only to changes in the relative angle of the catalyst relative to the surface.

Interferometric 2D SFG Spectra. Higher order spectroscopic techniques are complementary to linear spectroscopy and provide additional information because they separate contributions from inhomogeneous and homogeneous broadening and provide information on vibrational couplings. In particular, 2D SFG is a surface-specific fourth-order spectroscopy that provides vibrational and orientation information of molecules at interfaces,^{70,71} complementing other nonlinear techniques such as 2D IR^{59,60} or 2D ATR.^{62,63,66} We focus on the 2D SFG spectra of $\text{Re}(\text{CO})_3$ on nanocrystalline and crystalline TiO_2 surfaces to explore the spectroscopic response of the complex bound to different surfaces. Our recently developed implementation of interferometric 2D SFG provides a robust method that features high resolution in both frequency and temporal domains and exhibits high signal stability for molecular systems on transparent nonmetallic materials.⁷³

2D SFG can be performed with a narrow-band single-excitation pump–probe scheme,^{97,98} scanned across the frequency range of interest while the transient SFG spectrum is recorded. The time and frequency resolution of the experiment is restricted by the time-bandwidth product of the pump pulse. Alternatively, an interferometric version that employs two broad-band excitation pulses can be performed

with a pulse sequence shown in Figure 4.^{99–101} An interferogram in the recorded transient SFG spectrum is

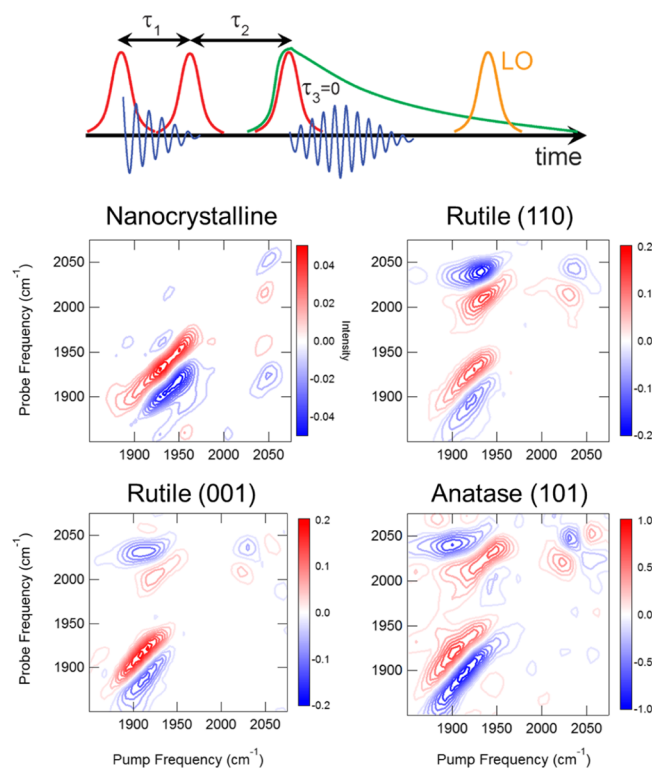


Figure 4. Top: Pulse sequence for interferometric 2D SFG. Bottom: 2D SFG spectrum of $\text{Re}(\text{CO})_3$ on nanocrystalline TiO_2 (upper left), single-crystal rutile (110) TiO_2 (upper right), rutile (001) TiO_2 (lower left), and anatase (101) TiO_2 (lower right), collected at a waiting time, τ_2 , of 0 ps. The contours are evenly spaced with blue indicating negative values and red indicating positive values.

obtained by scanning the time delay between the two broad-band pump pulses, τ_1 . The resulting interferogram is then Fourier-transformed to create the excitation axis with higher spectral and temporal resolution as set by the Fourier transform. Molecular dynamics can be monitored by varying the waiting time τ_2 between the pump and probe pulses. HD detection can be implemented in situ (for molecules bound to surfaces exhibiting a large nonresonant SFG response such as gold or crystalline quartz^{94,102}) or otherwise with an external LO^{73,95} to resolve the real and imaginary components of the signal without assuming a specific line shape.

Figure 4 shows the 2D SFG spectra of the $\text{Re}(\text{CO})_3$ complex on nanocrystalline TiO_2 , rutile (110) TiO_2 , rutile (001) TiO_2 , and anatase (101) TiO_2 with $\tau_2 = 0$ ps. The spectra are rather complex, with more structural and dynamic information than the corresponding 1D SFG spectra (Figure 3). Along the diagonal (pump frequency equal to probe frequency), opposite signs are observed for the fundamental transitions of the vibrational modes when compared to the peaks in the 1D spectrum. These features result from the reduced absorbance (bleach) of the fundamental transitions due to the pump pulses and thus carry the opposite sign than in the HD SFG spectrum. Because the HD SFG spectrum has positive (high frequency) and negative (low frequency) peaks, the resulting bleach peaks along the diagonal in the 2D SFG spectrum exhibit negative and positive features, respectively. Hence, 2D SFG provides more information than bulk 2D IR experiments

where all bleach features are negative because they are not sensitive to the absolute orientation of the molecule at the interface. Below each diagonal peak, there is a feature with opposite sign that corresponds to an induced absorbance from the $\nu = 1$ level. The frequency difference between these peaks provides information on the anharmonicity of the vibrational modes.

As shown in Figure 4, all 2D SFG spectra look qualitatively similar along the diagonal, consistent with FTIR and HD SFG spectra, with elongated antisymmetric peaks along the diagonal due to structural heterogeneity. The phase-twisted shape of the symmetric peak is likely due to improper phasing. Moreover, the elongated features suggest that inhomogeneous broadening is more significant than homogeneous broadening. Bulk 2D IR studies of TiO_2 nanoparticles have suggested that the heterogeneity could be partially due to aggregated molecules.⁹² However, Figure 4 shows no substructure in the symmetric stretch band of the complex on single crystals that could indicate aggregation, such as distinct intensities at slightly different vibrational frequencies within the symmetric stretch region.⁶⁸

The cross-peaks exhibit the most significant differences when comparing the spectra of $\text{Re}(\text{CO})_3$ on nanocrystalline and single-crystalline TiO_2 , reflecting differences in the anharmonic couplings between vibrational modes.⁵⁹ Furthermore, Figure 4 shows that the complex on nanocrystalline TiO_2 exhibits a cross-peak when probing the asymmetric stretch after excitation of the symmetric stretch, whereas no discernible cross-peak is observed when exciting and probing in reverse order. However, the opposite trend is observed for the complex on single crystals. In contrast, the bulk 2D IR spectrum with $\tau_2 = 0$ ps exhibits cross-peaks with equal intensities in the two quadrants, with asymmetries at longer times reflecting energy relaxation.⁵⁹ In 2D SFG, the intensities of the cross-peaks can be asymmetric because of several effects, including differences in the two coupled modes that provide further information on the molecular structure.¹⁰³

The asymmetric intensities of cross-peaks in the 2D SFG spectra, compared to symmetric cross-peaks in 2D IR, can be understood in terms of differences in cross-sections and selection rules of 2D SFG. Figure 5 shows a schematic diagram

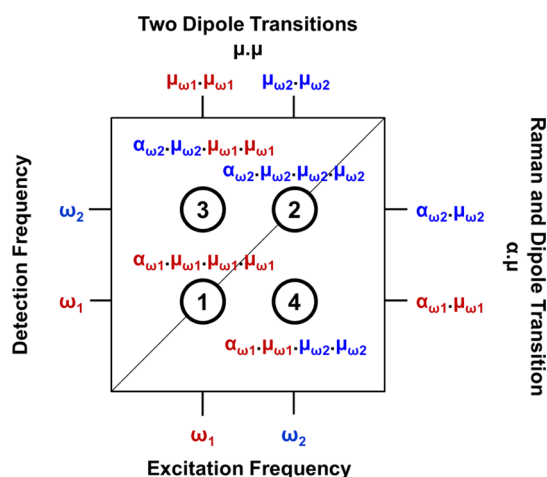


Figure 5. Schematic diagram of the 2D SFG spectrum for two coupled vibrational modes with frequencies ω_1 and ω_2 . Detection and excitation axes and contributions to each spectral feature are explicitly indicated.

of a 2D SFG spectrum for a system with two coupled vibrational modes with both diagonal and off-diagonal peaks. The excitation axis is generated by the interaction of the modes with two IR pulses and therefore involves two transition dipoles, $\mu\mu$. On the other hand, the detection axis is produced by Raman transition dipole, $\alpha\mu$, via the interaction with visible and third IR pulses. Hence, the detection features of 2D SFG must be SFG (both IR and Raman)-active, whereas the excitation requires only IR activity through a change in the transition dipole. These requirements are different from those of 2D IR spectroscopy where all four interactions of the modes are with IR pulses, involving four dipole transitions $\mu\mu\mu\mu$. Clearly, 2D SFG and 2D IR^{59,60} or 2D ATR^{62,63,66} provide complementary information.

Figure 5 shows that the intensity of each peak depends on the molecular interactions. Diagonal peaks are generated from interactions of one mode with the four pulses, whereas cross-peaks require that two modes interact with two pulses. Clearly, the cross-peaks are unequal if the corresponding diagonal peaks have different intensities. For example, when diagonal peak 1 is stronger than diagonal peak 2 due to a larger Raman transition, then, cross-peak 4 is larger than cross-peak 3. On the other hand, cross-peak 3 is stronger than cross-peak 4 when peak 1 is larger because of a larger dipole moment.

The HD spectra shown in Figure 3 indicate that the SFG peak of the symmetric stretch is stronger than the asymmetric stretch on single-crystalline TiO_2 ($\alpha_2\mu_2 > \alpha_1\mu_1$). Nevertheless, the IR intensities are similar (namely, $\mu_1 \approx \mu_2$), according to the FTIR spectrum of the immobilized catalyst (Figure 2). Such a difference contributes to a stronger cross-peak in the upper left quadrant of the 2D SFG spectrum. The opposite cross-peak trend is expected for the 2D data of the complex on nanocrystalline TiO_2 because the HD SFG spectra of the nanocrystalline system display a stronger asymmetric stretch band when compared to the symmetric stretch (namely, $\alpha_2\mu_2 < \alpha_1\mu_1$). In fact, these trends are observed in Figure 4, suggesting that the Raman and dipole transition strength differences likely contribute to both the uneven intensities of the cross-peaks and the lack of the upper cross-peak for the nanostructured surface, as observed within the signal-to-noise resolution of our experiments. We note that the absence of the lower frequency cross-peak for the single-crystalline surface is striking, particularly given the exceedingly strong upper cross-peak.

The above discussion is insightful although slightly oversimplified because the observed response arises from an average over an ensemble of molecular orientations. Furthermore, depending on the polarization of the pulses, different projections of the dipole moment and polarizability tensor contribute to the final spectrum. In this study, the IR and visible pulses are all p-polarized, so the obtained 2D SFG signals correspond to ppppp polarization. A p-polarized pulse interacts not only with the projection of the dipole moment or polarizability tensor normal to the surface (along the Z axis) but also with an in-plane projection (along the X axis). Hence, the final signal is a linear combination of different projections of the hyperpolarizability along the axis of the molecular frame. To understand the interplay between these different factors, we simulated the 2D SFG spectra of $\text{Re}(\text{CO})_3$ based on DFT calculations of hyperpolarizabilities (Figure 6). The analysis of the simulated spectra provides an understanding of the 2D SFG signals resulting from specific interactions and molecular orientations relative to the TiO_2 interface.

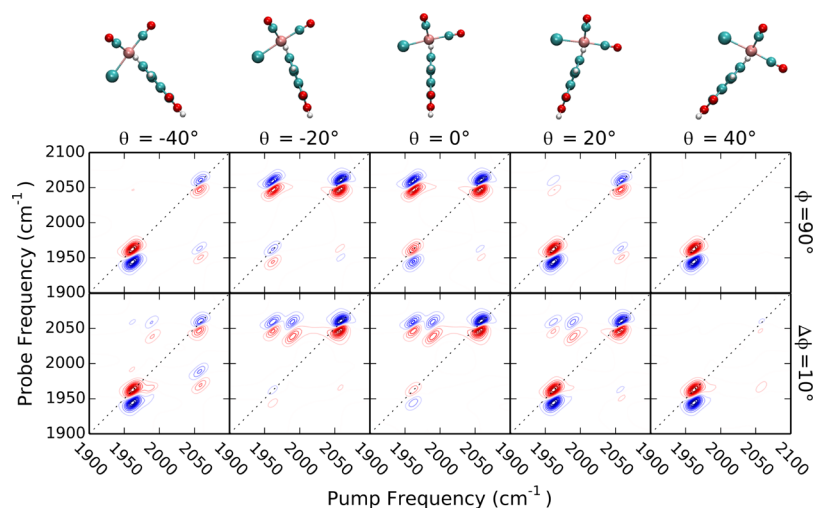


Figure 6. Ab initio 2D SFG spectra of the $\text{Re}(\text{CO})_3$ complex as a function of tilt angle θ for a bidentate binding motif ($\psi = 0^\circ$) and a delta distribution (top panel) or isotropic distribution (bottom panel) of the azimuthal angle ϕ . The spectra are normalized and correspond to zero waiting time ($\tau_2 = 0$ ps). The contours are evenly spaced with positive and negative values indicated in red and blue, respectively.

Ab Initio 2D SFG Spectra. We computed the 2D SFG spectra of the $\text{Re}(\text{CO})_3$ complex based on DFT hyperpolarizabilities. The calculated spectra provide insights on the origin of spectral changes induced by changes in the orientation of the complex relative to the TiO_2 surfaces. The methodology was built upon previous work on 1D SFG^{51,53,54,78} and 2D SFG,^{71,103} with details provided in the [Experimental Section](#). Briefly, the calculations involve computation of the 243 elements of the fourth-order hyperpolarizability tensor $\beta_{ijklm}^{(4)}$ at the DFT level. Subsequent rotation from the molecular to the laboratory frame (using Euler angles) provides the fourth-order susceptibility $\chi_{ijklm}^{(4)}$ (see [Experimental Section](#) for more detail). The spectrum is obtained as a linear combination of different elements of $\chi^{(4)}$ with coefficients that depend on the Fresnel factors of the interface and the incident angles of the beams. The simulations of 2D SFG spectra explicitly include the three CO modes with the anharmonic frequencies obtained by B3LYP/(SDD,6-311+G(d)) calculations.

[Figure 1](#) shows the optimized structure of the $\text{Re}(\text{CO})_3$ complex, along with the definition of the molecular axes (a , b , c) and laboratory frame (X , Y , Z). Here, ϕ is the azimuthal angle describing the rotation of the molecule relative to the normal to the TiO_2 surface, whereas θ describes the tilt of the bipyridine plane relative to the normal. The twist angle ψ describes the rotation of the complex along the c -axis. For simplicity, the line shape of each transition is modeled using Bloch dynamics with both homogeneous and inhomogeneous broadening parameters of 1 ps. These parameters could be fitted to reproduce the experimental line shapes but were kept constant because our goal was only to explore trends in the line shapes of the 2D SFG spectra as determined by changes in the orientation of the complex relative to the TiO_2 surface.

[Figure 6](#) (top panel) shows the ab initio 2D SFG spectra of the $\text{Re}(\text{CO})_3$ complex anchored to the surface through both carboxylate groups ($\psi = 0^\circ$) and azimuthal angle $\phi = 90^\circ$ as a function of the tilt angle θ (spectra for other azimuthal orientations are provided in the [Supporting Information](#)). The orientations shown in [Figure 6](#) correspond to the most stable configuration, subject to the constraint of fixed θ as determined by DFT⁵³ with the bidentate binding motif energetically

favorable on crystalline TiO_2 surfaces.^{51–53} The spectra include not only two diagonal bands but also two asymmetric cross-peaks with intensity ratios strongly modulated by the molecular orientation. As the molecule tilts, the upper diagonal peak is reduced, whereas the lower diagonal peak increases. The lower cross-peak can be very weak (or even absent) for an extended range of tilt angles θ around the surface normal, whereas the intensity of the upper cross-peak depends strongly on the orientation. We find that only very specific orientations reproduce the experimental pattern because small changes in the molecular orientation produce significant effects on both diagonal and cross-peaks, as determined by the higher sensitivity of the 2D response when compared to the 1D response.⁷¹ [Figure 6](#) shows that the DFT spectra are largely consistent with experiments, exhibiting an intense upper cross-peak and a very weak or absent lower cross-peak, when the molecule is perpendicular to the surface. Our results are also consistent with previous studies, suggesting that the complex binds to crystalline TiO_2 surfaces roughly normal perpendicular, with a tilt angle θ ranging from 0 to 30° .^{51,53} The agreement supports the DFT simulations as valuable tools for rigorous interpretation of 2D SFG spectra.

So far, we have limited the analysis to a predominant configuration of the azimuthal angle responsible for the response. However, multiple configurations likely contribute to the signal.⁷ Therefore, it is necessary to perform an average of the susceptibility $\chi_{ijklm}^{(4)}$ tensor over the distribution of thermal configurations (see [Experimental Section](#)). [Figure 6](#) (bottom panel) shows the azimuthally-averaged SFG spectra of $\text{Re}(\text{CO})_3$ with different tilt angles, assuming an isotropic distribution over configurations lying 10° apart ($\Delta\phi = 10^\circ$). Azimuthally averaged spectra, consistent with the symmetry of rutile (001) TiO_2 and rutile (110) TiO_2 surfaces, are similar, as shown in [Supporting Information](#).

[Figure 6](#) (bottom panel) shows that the main trends drawn from calculations based on a predominant configuration of the azimuthal angle also hold true for averages over wider distributions of orientations. The intense upper cross-peak and the missing lower cross-peak agree with experiments ([Figure 4](#)) so long as the $\text{Re}(\text{CO})_3$ complex is oriented normal to the surface (or close to the normal).

We decomposed the overall response according to the various contributions from different $\chi^{(4)}$ elements to gain insight into the origin of the spectral features. For the all-p polarization experiment (ppppp), the response results from a combination of different $\chi^{(4)}$ tensor elements weighted by the Fresnel factors of the sample (see Experimental Section). On metal surfaces, where the Fresnel factor is strong in the Z direction, the ppppp spectra are dominated by the χ_{ZZZZZ} element.^{54,96} Nevertheless, all of the (symmetry-allowed) elements contribute to the final line shape of adsorbates on TiO₂ (see Table S1). The transition dipole moment of the symmetric stretch projects mainly along the normal to the surface, whereas the asymmetric modes are almost perpendicular to the symmetric stretch. Therefore, different components of polarized light interact with different modes, giving rise to a distinct response.

Figure 7 shows representative examples of individual contributions to the ppppp 2D SFG signal resulting from

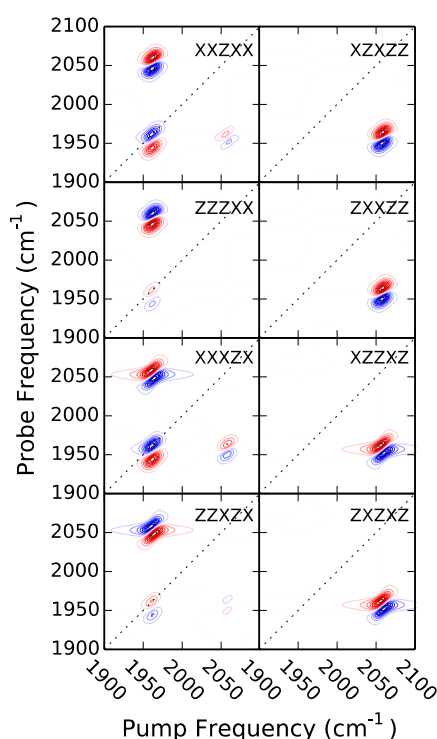


Figure 7. Individual contributions to the ppppp 2D SFG spectra from selected elements of the $\chi^{(4)}$ tensor as determined by DFT calculations for zero waiting time ($\tau_2 = 0$ ps). All spectra correspond to a configuration with $\theta = 0^\circ$ and $\phi = 90^\circ$. The spectra are normalized. The contours are evenly spaced with blue and red indicating negative and positive values, respectively.

selected $\chi^{(4)}$ elements. The right panels correspond to the $\chi^{(4)}$ elements that provide a major contribution to the lower cross-peak. The signal is generated by the interaction of the IR pump pulse with the Z component of the symmetric stretch transition dipole moment, probing the transition dipole and polarizability parameters of the asymmetric stretch (see peak 4 in Figure 5). Because $\alpha_{XZ} = \alpha_{ZX}$, responses that “share” the same IR pulse sequence (e.g., XZXZZ and ZXXZZ polarizations) exhibit the *same* line shapes. Moreover, the responses shown in Figure 7 (right panels) interfere *destructively* with each other in the final ppppp spectra, producing a very small signal in the lower cross-peak region because the coefficients

associated with light emitted in the X direction are comparable magnitude but opposite sign to those associated with the Z direction in the linear combination of elements of $\chi^{(4)}$ (Table S1).

For the upper cross-peak, the situation is just the opposite. Figure 7 (left panels) shows $\chi^{(4)}$ elements that contribute to the upper region. These signals arise from pumping the asymmetric stretch via the X component of the transition dipole moment and probing elements of the high-frequency mode (see Figure 5). Elements of $\chi^{(4)}$ that have the same IR pulse sequences exhibit *different* responses because $\alpha_{XX} \neq \alpha_{ZZ}$. More importantly, they exhibit constructive interference in the final absorptive spectra because of the sign of the linear coefficients, resulting in an intense upper cross-peak.

The overall conclusion that emerges from this analysis is, then, that destructive (constructive) interference between different elements of $\chi^{(4)}$ suppresses (or enhance) the lower (or upper) cross-peak signal, as determined by the particular state of polarization of the light and the strength of the dipole transition and polarizability of each mode.

The destructive interference suppressing the lower cross-peak is determined by the specific linear combination of elements of the $\chi^{(4)}$ tensor. Therefore, the spectra depend strongly on the type of polarization scheme used in the experiment. As a matter of fact, by changing the polarization of the pulses, it is possible to emphasize different types of signals and even eliminate diagonal peaks.⁷¹ Figure 8 illustrates that observation by showing the calculated 2D SFG spectra predicted for other polarizations, including the comparison

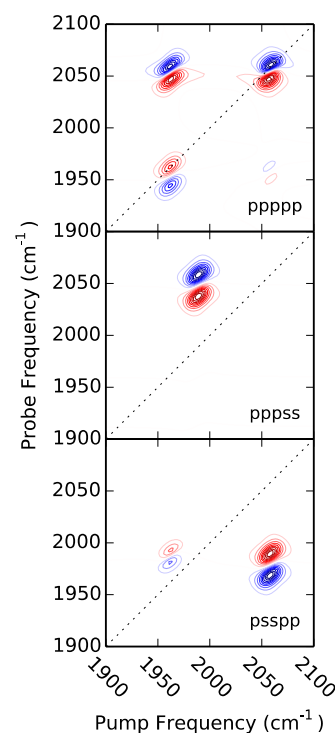


Figure 8. Ab initio 2D SFG spectra for various polarization schemes, including ppppp, pppss, and psspp. The spectra correspond to a configuration with $\theta = 0^\circ$ and $\phi = 90^\circ$. The ratio of maximum intensities of ppppp/pppss/psspp spectra is 8:4:1. All spectra are normalized and correspond to zero waiting time. The contours are evenly spaced with blue and red indicating negative and positive values, respectively.

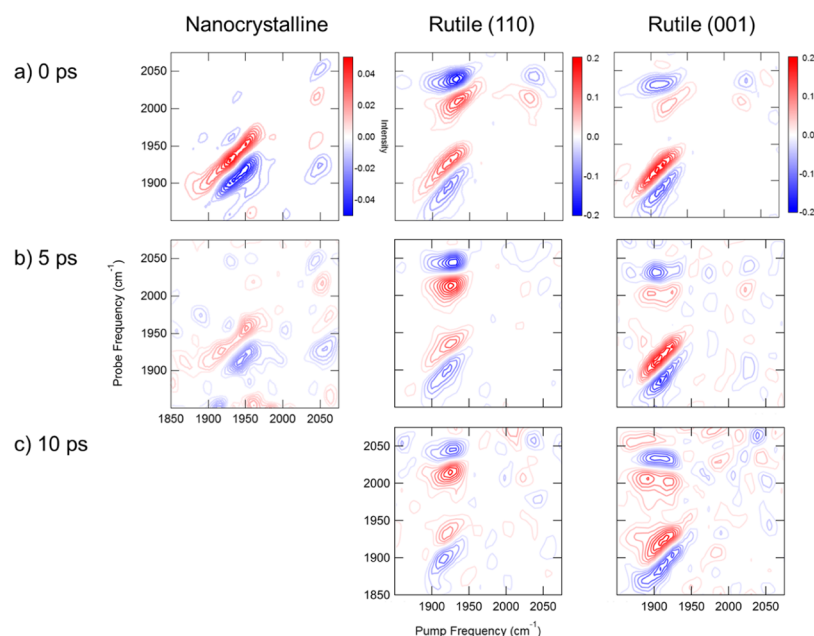


Figure 9. 2D SFG spectra of $\text{Re}(\text{CO})_3$ on nanocrystalline TiO_2 , rutile (110) TiO_2 , and rutile (001) TiO_2 surfaces, as a function of the waiting time τ_2 between pump and probe pulses.

of ppppp, pppss, and psspp for the most stable configuration of the complex. The use of s-polarized IR pump pulses excites only modes with dipole moments parallel to the surfaces (asymmetric modes), whereas probing the system in the p polarization triggers responses from the symmetric mode, perpendicular to the asymmetric stretch. Hence, the pppss polarization enhances the signal for the upper cross-peak. On the other hand, probing in the s polarization and pumping in the p polarization with the psspp sequence enhances the lower cross-peak (Figure 8). Note that although the intensity of the signal is less intense than in the all-p spectrum (e.g., the ratio of intensities of ppppp/pppss/psspp spectra is 8:4:1), it should still be possible to measure the spectra with various polarization schemes with reasonable signal-to-noise ratio to obtain additional information on the couplings and dynamics of catalysts such as $\text{Re}(\text{CO})_3$ on TiO_2 surfaces. We note in passing that the cross-peaks in Figure 8 appear at a different location for pppss and psspp in comparison to the cross-peaks of the ppppp polarization because in the former, only the A'' asymmetric mode is predominantly excited by the s-polarized IR field, whose frequency is slightly shifted from the one of the $A'(2)$ asymmetric mode that is mostly excited in the ppppp experiment. Note that this feature, which can be already observed in the bottom panels of Figure 6, is an artifact of the calculation because of the somewhat overestimated separation of the DFT frequency for the asymmetric stretching modes and is unlikely to be observed in experiments where the two asymmetric peaks are not resolved (see Figure 4).

Vibrational Relaxation. Having analyzed the static properties of $\text{Re}(\text{CO})_3$ on different TiO_2 surfaces, here, we characterize the dynamical behavior of the complex. In a 2D SFG experiment, the first two IR pulses “label” a particular vibrational mode by storing the frequency information in the pump axis, whereas the third IR and Vis pulses are used to “read out” the molecular frequency information reflected in the probe axis. Between the pump and probe pulses, the molecule fluctuates and the probe vibrational frequency evolves, accordingly. Therefore, by changing the delay time τ_2 between

the pump IR pulses and the probe IR/vis pulses (see scheme of pulse sequence in Figure 4), it is possible to follow the dynamical evolution of a particular probe vibration and obtain information of the vibrational relaxation pathway, spectral diffusion, and structural evolution.

Figure 9 shows the 2D SFG spectra of $\text{Re}(\text{CO})_3$ on nanocrystalline and single-crystal TiO_2 for waiting times $\tau_2 = 0, 5$, and 10 ps. Multiple waiting times were not measured for the anatase (101) surface because the compound degraded over time under laser radiation. For the nanocrystalline surfaces, strong diagonal features decayed with increasing waiting time because of vibrational relaxation with a substructure that persisted at 5 ps likely due to structural heterogeneity.⁷³ For the crystalline surfaces, the spectra were qualitatively different. For rutile (110), the diagonal peak of the high-frequency symmetric mode relaxed within 5 ps, whereas the strong cross-peak with the antisymmetric modes decayed much more slowly and was still observed at 10 ps. The symmetric stretch decayed similarly on rutile (001), although more slowly than on rutile (110).

The vibrational relaxation timescale for the symmetric stretch mode of carbonyl is 18 ps on rutile (110) and 26 ps on the (001) surface as obtained by SFG pump–probe experiments.⁷⁵ The pump–probe signal at a given waiting time is obtained from a 2D SFG spectrum by integrating the spectrum along the excitation axis, thereby summing diagonal and off-diagonal features.⁵⁹ Normally, off-diagonal peaks are significantly weaker than diagonal peaks and pump–probe spectra are dominated by the diagonal features. Therefore, the observed relaxation dynamics in pump–probe experiments usually reflect the relaxation of the vibrational mode at the given frequency. Figure 9 shows that this is indeed the case for $\text{Re}(\text{CO})_3$ on nanocrystalline TiO_2 . However, for single-crystalline surfaces, the faster relaxation of the diagonal peak and the persistence of the cross-peak at 10 ps suggest that the cross-peak of pump–probe experiments is actually probing the longer vibrational relaxation of the lower frequency asymmetric modes. Such observation highlights the capabilities of 2D

experiments to reveal previously obscured information, including vibrational relaxation timescales from pump–probe spectra.

The overall picture that emerges from our analysis of 2D SFG spectra is that the vibrational relaxation of the $\text{Re}(\text{CO})_3$ catalyst on single-crystalline surfaces is dramatically different on single crystals or nanocrystalline surfaces. The bound catalyst exhibits a subpicosecond redistribution of the vibrational energy between the symmetric and asymmetric modes, which decay together on the tens of picosecond timescale.⁵⁶ The symmetric vibration of the catalyst on single-crystalline surfaces relaxes unidirectionally within a few ps into the asymmetric mode that then decays on the tens of picosecond time scale. These observations reveal that the dynamical properties and vibrational couplings are very different on single-crystalline and nanostructured surfaces. Because the vibrational lifetime on the nanostructured surface is comparable to the delay between excitation and electron injection into TiO_2 ,²⁹ the vibrational relaxation likely modulates the electron injection rate. Accordingly, changes in the vibrational relaxation dynamics likely influence charge injection and catalytic performance. Furthermore, the CO vibrational modes report on the electronic structure of the Re center. Therefore, the redox behavior of the catalyst is most likely different on single-crystalline and nanostructured surfaces.

The development of faceted nanostructures to increase conversion efficiency is a subject of great practical interest.^{30–38} Catalysts bound on faceted surfaces are expected to exhibit similar behavior as when bound to single-crystalline surfaces. Therefore, our finding of different dynamical and structural properties of the catalyst on single-crystalline surfaces is relevant to the design of catalytic materials with faceted surfaces as well as for understanding the distinct catalytic performance exhibited by different faceted nanostructures. Furthermore, considering the structural similarities of the $\text{Re}(\text{CO})_3$ catalyst and dyes commonly used in dye-sensitized solar cells, we anticipated that the reported findings should also be valuable for understanding differences in solar photoconversion efficiencies as observed on various single-crystalline surfaces.^{15–25}

CONCLUSIONS

We have investigated the effect of different TiO_2 surfaces on the vibrational relaxation dynamics and binding mode of $\text{Re}(\text{CO})_3$ catalysts by combining interferometric 2D SFG spectroscopy and DFT simulations of 2D SFG spectra. We find that the properties of the catalyst are quite different on single-crystal TiO_2 surfaces when compared to a nanocrystalline TiO_2 system in terms of molecular orientation, vibrational relaxation dynamics, and vibrational coupling.

The analysis of the 2D spectra revealed a striking difference between single-crystal and nanocrystalline TiO_2 where different cross-peak patterns are observed. We found that for the crystalline surfaces, a cross-peak is observed when exciting the asymmetric stretch and probing the symmetric stretch, whereas no signal is detected in the reverse sequence. The opposite is observed for the nanoparticle surface. By comparing experimental and DFT-based 2D SFG spectra and decomposing the ab initio spectra into the different elements contributing to the complex signal, we found that the origin of spectroscopic differences can be traced back to the ordered nature of the catalyst bound to single-crystalline surfaces,

resulting in destructive interference between certain $\chi^{(4)}$ elements due to the all-p polarization scheme and the strength of the correlation between the transition dipole and polarizability for each mode of the catalyst oriented normal to the surface.

We have analyzed the dynamical behavior of the catalyst on rutile (110) by monitoring the vibrational energy in the $A'(1)$ mode that relaxes rather quickly (within 5 ps) by energy transfer to the low-frequency modes. The symmetric mode also decays quickly on rutile (001) in contrast to the much slower relaxation dynamics observed on nanocrystalline TiO_2 , comparable to the relaxation dynamics of the catalyst in the bulk solution. The difference is likely due to the stronger vibrational coupling of ordered monolayers on single-crystalline surfaces when compared to the corresponding couplings for the complex on nanocrystalline TiO_2 . Therefore, we conclude that $\text{Re}(\text{CO})_3$ exhibits distinct structural and dynamical properties when bound to TiO_2 single crystals or nanostructured surfaces, likely due to distinct molecular arrangements on different surfaces. Although the catalyst forms a disordered film on nanocrystalline TiO_2 , an ordered film is formed on single crystals, as evident from the cross-peak pattern in the 2D SFG spectra, leading to distinct vibrational relaxation pathways.

We anticipate that the observed differences in relaxation dynamics could correlate with different efficiencies of catalytic functionality. In particular, the rutile (110) surface should be better than rutile (001) for catalytic reactions where the TiO_2 surface functions as an electron sink after vibrational relaxation. The anatase (101) surface should exhibit intermediate performance, less effective than rutile (110). In addition, the carbonyl ligands modulate the redox properties of the Re center through π back-bonding interactions, and therefore, differences in CO vibrational relaxation are expected to have an influence on the catalytic cycle of CO_2 reduction.

Understanding the distinct environment surrounding the $\text{Re}(\text{CO})_3$ catalyst bound to different surfaces is particularly valuable for the design and optimization of catalytic materials. In particular, for catalysts with faceted nanostructures of high surface area of great current interest for enhanced performance. Catalysts bound to faceted nanostructures will likely exhibit properties similar to those of single-crystalline surfaces. According to our findings, colloidal nanostructured surfaces are not sufficiently a good model of emerging faceted nanostructures for the solar energy conversion. More realistic models of faceted nanostructures are catalysts bound to single-crystalline surfaces. Those models can be readily explored by interferometric 2D SFG spectroscopy combined with DFT simulations, a powerful combination that provides unique structural and dynamic information of catalytic monolayers.

ASSOCIATED CONTENT

Supporting Information

The Supporting Information is available free of charge on the ACS Publications website at DOI: 10.1021/acs.jpcc.8b08423.

Optimized coordinates, dipoles derivatives, and polarizabilities derivatives of the $\text{Re}(\text{CO})_3$ complex used for the calculation of ab initio 2D SFG spectra (PDF)

AUTHOR INFORMATION

Corresponding Authors

*E-mail: victor.batista@yale.edu (V.S.B.).

*E-mail: pbp33@cornell.edu (P.B.P.).

ORCID

Heather Vanselow: 0000-0002-7868-3900

Pablo E. Videla: 0000-0003-0742-0342

Victor S. Batista: 0000-0002-3262-1237

Poul B. Petersen: 0000-0002-9821-700X

Author Contributions

[§]H.V. and P.E.V. contributed equally.

Notes

The authors declare no competing financial interest.

ACKNOWLEDGMENTS

This work was supported by the National Science Foundation under a NSF CAREER grant (CHE-1151079 to P.B.P.) and the Air Force Office of Scientific Research (FA9550-17-0198 to V.S.B.). This work made use of the Cornell Center for Materials Research Shared Facilities which are supported through the NSF MRSEC program (DMR-1719875). V.S.B. acknowledges supercomputing time from NERSC and from the Yale High Performance Computing Center. The authors would like to thank Jian Cheng Wong for help with preparing the nanocrystalline TiO₂ sample. The authors would like to thank Benjamin Rudshteyn for helpful advice and discussion and for help in editing a preliminary version of the manuscript.

REFERENCES

- (1) Moore, G. F.; Brudvig, G. W. Energy Conversion in Photosynthesis: A Paradigm for Solar Fuel Production. *Annu. Rev. Condens. Matter Phys.* **2011**, *2*, 303–327.
- (2) Berardi, S.; Drouet, S.; Francàs, L.; Gimbert-Suriñach, C.; Guttentag, M.; Richmond, C.; Stoll, T.; Llobet, A. Molecular Artificial Photosynthesis. *Chem. Soc. Rev.* **2014**, *43*, 7501–7519.
- (3) Garrido-Barros, P.; Gimbert-Suriñach, C.; Moonshiram, D.; Picón, A.; Monge, P.; Batista, V. S.; Llobet, A. Electronic π -Delocalization Boosts Catalytic Water Oxidation by Cu(I) Molecular Catalysts Heterogenized on Graphene Sheets. *J. Am. Chem. Soc.* **2017**, *139*, 12907–12910.
- (4) Sheehan, S. W.; Thomsen, J. M.; Hintermair, U.; Crabtree, R. H.; Brudvig, G. W.; Schmuttenmaer, C. A. A Molecular Catalyst for Water Oxidation That Binds to Metal Oxide Surfaces. *Nat. Commun.* **2015**, *6*, 6469.
- (5) Materna, K. L.; Rudshteyn, B.; Brennan, B. J.; Kane, M. H.; Bloomfield, A. J.; Huang, D. L.; Shopov, D. Y.; Batista, V. S.; Crabtree, R. H.; Brudvig, G. W. Heterogenized Iridium Water-Oxidation Catalyst from a Silatrane Precursor. *ACS Catal.* **2016**, *6*, 5371–5377.
- (6) Materna, K. L.; Crabtree, R. H.; Brudvig, G. W. Anchoring Groups for Photocatalytic Water Oxidation on Metal Oxide Surfaces. *Chem. Soc. Rev.* **2017**, *46*, 6099–6110.
- (7) Anuso, C. L.; Snoberger, R. C.; Ricks, A. M.; Liu, W.; Xiao, D.; Batista, V. S.; Lian, T. Covalent Attachment of a Rhenium Bipyridyl CO₂ Reduction Catalyst to Rutile TiO₂. *J. Am. Chem. Soc.* **2011**, *133*, 6922–6925.
- (8) Oh, S.; Gallagher, J. R.; Miller, J. T.; Surendranath, Y. Graphite-Conjugated Rhenium Catalysts for Carbon Dioxide Reduction. *J. Am. Chem. Soc.* **2016**, *138*, 1820–1823.
- (9) Schreier, M.; Luo, J.; Gao, P.; Moehl, T.; Mayer, M. T.; Grätzel, M. Covalent Immobilization of a Molecular Catalyst on Cu₂O Photocathodes for CO₂ Reduction. *J. Am. Chem. Soc.* **2016**, *138*, 1938–1946.
- (10) Liu, C.; Dubois, K. D.; Louis, M. E.; Vorushilov, A. S.; Li, G. Photocatalytic CO₂ Reduction and Surface Immobilization of a Tricarbonyl Re(I) Compound Modified with Amide Groups. *ACS Catal.* **2013**, *3*, 655–662.

- (11) Kumar, B.; Llorente, M.; Froehlich, J.; Dang, T.; Sathrum, A.; Kubiak, C. P. Photochemical and Photoelectrochemical Reduction of CO₂. *Annu. Rev. Phys. Chem.* **2012**, *63*, 541–569.
- (12) Fujishima, A.; Rao, T. N.; Tryk, D. A. Titanium Dioxide Photocatalysis. *J. Photochem. Photobiol., C* **2000**, *1*, 1–21.
- (13) Diebold, U. The Surface Science of Titanium Dioxide. *Surf. Sci. Rep.* **2003**, *48*, 53–229.
- (14) Windle, C. D.; Pastor, E.; Reynal, A.; Whitwood, A. C.; Vaynzof, Y.; Durrant, J. R.; Perutz, R. N.; Reisner, E. Improving the Photocatalytic Reduction of CO₂ to CO through Immobilisation of a Molecular Re Catalyst on TiO₂. *Chem. - Eur. J.* **2015**, *21*, 3746–3754.
- (15) Spitler, M. T.; Parkinson, B. A. Dye Sensitization of Single Crystal Semiconductor Electrodes. *Acc. Chem. Res.* **2009**, *42*, 2017–2029.
- (16) Lu, Y.; Choi, D.-j.; Nelson, J.; Yang, O.-B.; Parkinson, B. A. Adsorption, Desorption, and Sensitization of Low-Index Anatase and Rutile Surfaces by the Ruthenium Complex Dye N3. *J. Electrochem. Soc.* **2006**, *153*, E131.
- (17) Yang, H. G.; Sun, C. H.; Qiao, S. Z.; Zou, J.; Liu, G.; Smith, S. C.; Cheng, H. M.; Lu, G. Q. Anatase TiO₂ Single Crystals with a Large Percentage of Reactive Facets. *Nature* **2008**, *453*, 638–641.
- (18) Liu, G.; Yu, J. C.; Lu, G. Q.; Cheng, H.-M. Crystal Facet Engineering of Semiconductor Photocatalysts: Motivations, Advances and Unique Properties. *Chem. Commun.* **2011**, *47*, 6763–6783.
- (19) Wu, X.; Chen, Z.; Lu, G. Q. M.; Wang, L. Nanosized Anatase TiO₂ Single Crystals with Tunable Exposed (001) Facets for Enhanced Energy Conversion Efficiency of Dye-Sensitized Solar Cells. *Adv. Funct. Mater.* **2011**, *21*, 4167–4172.
- (20) Lin, H.; Li, L.; Zhao, M.; Huang, X.; Chen, X.; Li, G.; Yu, R. Synthesis of High-Quality Brookite TiO₂ Single-Crystalline Nano-sheets with Specific Facets Exposed: Tuning Catalysts from Inert to Highly Reactive. *J. Am. Chem. Soc.* **2012**, *134*, 8328–8331.
- (21) Tachikawa, T.; Yamashita, S.; Majima, T. Evidence for Crystal-Face-Dependent TiO₂ Photocatalysis from Single-Molecule Imaging and Kinetic Analysis. *J. Am. Chem. Soc.* **2011**, *133*, 7197–7204.
- (22) Yu, J.; Low, J.; Xiao, W.; Zhou, P.; Jaroniec, M. Enhanced Photocatalytic CO₂-Reduction Activity of Anatase TiO₂ by Coexposed {001} and {101} Facets. *J. Am. Chem. Soc.* **2014**, *136*, 8839–8842.
- (23) Ong, W.-J.; Tan, L.-L.; Chai, S.-P.; Yong, S.-T.; Mohamed, A. R. Facet-Dependent Photocatalytic Properties of TiO₂-Based Composites for Energy Conversion and Environmental Remediation. *ChemSusChem* **2014**, *7*, 690–719.
- (24) Li, C.; Koenigsmann, C.; Ding, W.; Rudshteyn, B.; Yang, K. R.; Regan, K. P.; Konezny, S. J.; Batista, V. S.; Brudvig, G. W.; Schmuttenmaer, C. A.; Kim, J.-H. Facet-Dependent Photoelectrochemical Performance of TiO₂ Nanostructures: An Experimental and Computational Study. *J. Am. Chem. Soc.* **2015**, *137*, 1520–1529.
- (25) Guo, Q.; Zhou, C.; Ma, Z.; Ren, Z.; Fan, H.; Yang, X. Elementary Photocatalytic Chemistry on TiO₂ Surface. *Chem. Soc. Rev.* **2016**, *45*, 3701–3730.
- (26) Cecchet, F.; Alebbi, M.; Bignozzi, C. A.; Paolucci, F. Efficiency Enhancement of the Electrocatalytic Reduction of CO₂: Fac-[Re(V-Bpy)(Co)3cl] Electropolymerized onto Mesoporous TiO₂ Electrodes. *Inorg. Chim. Acta* **2006**, *359*, 3871–3874.
- (27) Takeda, H.; Ohashi, M.; Tani, T.; Ishitani, O.; Inagaki, S. Enhanced Photocatalysis of Rhenium(I) Complex by Light-Harvesting Periodic Mesoporous Organosilica. *Inorg. Chem.* **2010**, *49*, 4554–4559.
- (28) Liu, C.; Dubois, K. D.; Louis, M. E.; Vorushilov, A. S.; Li, G. Photocatalytic CO₂ Reduction and Surface Immobilization of a Tricarbonyl Re (I) Compound Modified with Amide Groups. *ACS Catal.* **2013**, *3*, 655–662.
- (29) Abdellah, M.; El-Zohry, A. M.; Antila, L. J.; Windle, C. D.; Reisner, E.; Hammarström, L. Time-Resolved Ir Spectroscopy Reveals a Mechanism with TiO₂ as a Reversible Electron Acceptor in a TiO₂–Re Catalyst System for CO₂ Photoreduction. *J. Am. Chem. Soc.* **2017**, *139*, 1226–1232.

- (30) Miao, L.; Tanemura, S.; Toh, S.; Kaneko, K.; Tanemura, M. Fabrication, characterization and Raman study of anatase-TiO₂ nanorods by a heating-sol-gel template process. *J. Cryst. Growth* **2004**, *264*, 246–252.
- (31) Liu, B.; Aydil, E. S. Growth of Oriented Single-Crystalline Rutile TiO₂ Nanorods on Transparent Conducting Substrates for Dye-Sensitized Solar Cells. *J. Am. Chem. Soc.* **2009**, *131*, 3985–3990.
- (32) Li, Y.; Guo, M.; Zhang, M.; Wang, X. Hydrothermal Synthesis and Characterization of TiO₂ Nanorod Arrays on Glass Substrates. *Mater. Res. Bull.* **2009**, *44*, 1232–1237.
- (33) Wang, S.-M.; Dong, W.-W.; Tao, R.-H.; Deng, Z.-H.; Shao, J.-Z.; Hu, L.-H.; Zhu, J.; Fang, X.-D. Optimization of Single-Crystal Rutile TiO₂ Nanorod Arrays Based Dye-Sensitized Solar Cells and Their Electron Transport Properties. *J. Power Sources* **2013**, *235*, 193–201.
- (34) Huang, H.; Pan, L.; Lim, C. K.; Gong, H.; Guo, J.; Tse, M. S.; Tan, O. K. Hydrothermal Growth of TiO₂ Nanorod Arrays and in Situ Conversion to Nanotube Arrays for Highly Efficient Quantum Dot-Sensitized Solar Cells. *Small* **2013**, *9*, 3153–3160.
- (35) Zhang, W.; Xie, Y.; Xiong, D.; Zeng, X.; Li, Z.; Wang, M.; Cheng, Y.-B.; Chen, W.; Yan, K.; Yang, S. TiO₂ Nanorods: A Facile Size- and Shape-Tunable Synthesis and Effective Improvement of Charge Collection Kinetics for Dye-Sensitized Solar Cells. *ACS Appl. Mater. Interfaces* **2014**, *6*, 9698–9704.
- (36) Jarosz, M.; Syrek, K.; Kapusta-Kolodziej, J.; Mech, J.; Małek, K.; Hnida, K.; Łojewski, T.; Jaskuła, M.; Sulka, G. D. Heat Treatment Effect on Crystalline Structure and Photoelectrochemical Properties of Anodic TiO₂ Nanotube Arrays Formed in Ethylene Glycol and Glycerol Based Electrolytes. *J. Phys. Chem. C* **2015**, *119*, 24182–24191.
- (37) Fakharuddin, A.; Di Giacomo, F.; Palma, A. L.; Matteocci, F.; Ahmed, I.; Razza, S.; D'Epifanio, A.; Licocchia, S.; Ismail, J.; Di Carlo, A.; Brown, T. M.; Jose, R. Vertical TiO₂ Nanorods as a Medium for Stable and High-Efficiency Perovskite Solar Modules. *ACS Nano* **2015**, *9*, 8420–8429.
- (38) Guo, W.; Xu, C.; Wang, X.; Wang, S.; Pan, C.; Lin, C.; Wang, Z. L. Rectangular Bunched Rutile TiO₂ Nanorod Arrays Grown on Carbon Fiber for Dye-Sensitized Solar Cells. *J. Am. Chem. Soc.* **2012**, *134*, 4437–4441.
- (39) Hawecker, J.; Lehn, J.-M.; Ziessel, R. Electrocatalytic Reduction of Carbon Dioxide Mediated by Re(Bipy)(Co)₃Cl (Bipy = 2,2'-Bipyridine). *J. Chem. Soc., Chem. Commun.* **1984**, 328–330.
- (40) Smieja, J. M.; Kubiak, C. P. Re(Bipy-Tbu)(Co)₃Cl—Improved Catalytic Activity for Reduction of Carbon Dioxide: Ir-Spectroelectrochemical and Mechanistic Studies. *Inorg. Chem.* **2010**, *49*, 9283–9289.
- (41) Sampson, M. D.; Froehlich, J. D.; Smieja, J. M.; Benson, E. E.; Sharp, I. D.; Kubiak, C. P. Direct Observation of the Reduction of Carbon Dioxide by Rhenium Bipyridine Catalysts. *Energy Environ. Sci.* **2013**, *6*, 3748–3755.
- (42) Takeda, H.; Koike, K.; Inoue, H.; Ishitani, O. Development of an Efficient Photocatalytic System for CO₂ Reduction Using Rhenium(I) Complexes Based on Mechanistic Studies. *J. Am. Chem. Soc.* **2008**, *130*, 2023–2031.
- (43) Windle, C. D.; Pastor, E.; Reynal, A.; Whitwood, A. C.; Vaynzof, Y.; Durrant, J. R.; Perutz, R. N.; Reisner, E. Improving the Photocatalytic Reduction of CO₂ to CO through Immobilisation of a Molecular Re Catalyst on TiO₂. *Chem.—Eur. J.* **2015**, *21*, 3746–3754.
- (44) Kiefer, L. M.; Kubarych, K. J. Solvent-Dependent Dynamics of a Series of Rhenium Photoactivated Catalysts Measured with Ultrafast 2dir. *J. Phys. Chem. A* **2015**, *119*, 959–965.
- (45) Kiefer, L. M.; King, J. T.; Kubarych, K. J. Equilibrium Excited State Dynamics of a Photoactivated Catalyst Measured with Ultrafast Transient 2dir. *J. Phys. Chem. A* **2014**, *118*, 9853–9860.
- (46) Kiefer, L. M.; Kubarych, K. J. Solvent Exchange in Preformed Photocatalyst-Donor Precursor Complexes Determines Efficiency. *Chem. Sci.* **2018**, *9*, 1527–1533.
- (47) Kiefer, L. M.; King, J. T.; Kubarych, K. J. Dynamics of Rhenium Photocatalysts Revealed through Ultrafast Multidimensional Spectroscopy. *Acc. Chem. Res.* **2015**, *48*, 1123–1130.
- (48) Asbury, J. B.; Wang, Y.; Lian, T. Time-Dependent Vibration Stokes Shift During Solvation: Experiment and Theory. *Bull. Chem. Soc. Jpn.* **2002**, *75*, 973–983.
- (49) Dattelbaum, D. M.; Omberg, K. M.; Schoonover, J. R.; Martin, R. L.; Meyer, T. J. Application of Time-Resolved Infrared Spectroscopy to Electronic Structure in Metal-to-Ligand Charge-Transfer Excited States. *Inorg. Chem.* **2002**, *41*, 6071–6079.
- (50) Asbury, J. B.; Hao, E.; Wang, Y.; Ghosh, H. N.; Lian, T. Ultrafast Electron Transfer Dynamics from Molecular Adsorbates to Semiconductor Nanocrystalline Thin Films. *J. Phys. Chem. B* **2001**, *105*, 4545–4557.
- (51) Anfuso, C. L.; Snoeberger, R. C.; Ricks, A. M.; Liu, W.; Xiao, D.; Batista, V. S.; Lian, T. Covalent Attachment of a Rhenium Bipyridyl CO₂ Reduction Catalyst to Rutile TiO₂. *J. Am. Chem. Soc.* **2011**, *133*, 6922–6925.
- (52) Anfuso, C. L.; Xiao, D.; Ricks, A. M.; Negre, C. F. A.; Batista, V. S.; Lian, T. Orientation of a Series of CO₂ Reduction Catalysts on Single Crystal TiO₂ Probed by Phase-Sensitive Vibrational Sum Frequency Generation Spectroscopy (Ps-Vsfg). *J. Phys. Chem. C* **2012**, *116*, 24107–24114.
- (53) Ge, A.; Rudshiteyn, B.; Psciuk, B. T.; Xiao, D.; Song, J.; Anfuso, C. L.; Ricks, A. M.; Batista, V. S.; Lian, T. Surface-Induced Anisotropic Binding of a Rhenium CO₂-Reduction Catalyst on Rutile TiO₂ (110) Surfaces. *J. Phys. Chem. C* **2016**, *120*, 20970–20977.
- (54) Clark, M. L.; Rudshiteyn, B.; Ge, A.; Chabolla, S. A.; Machan, C. W.; Psciuk, B. T.; Song, J.; Canzi, G.; Lian, T.; Batista, V. S.; Kubiak, C. P. Orientation of Cyano-Substituted Bipyridine Re(I) Fac-Tricarbonyl Electrocatalysts Bound to Conducting Au Surfaces. *J. Phys. Chem. C* **2016**, *120*, 1657–1665.
- (55) Anfuso, C. L.; Ricks, A. M.; Rodríguez-Córdoba, W.; Lian, T. Ultrafast Vibrational Relaxation Dynamics of a Rhenium Bipyridyl CO₂-Reduction Catalyst at a Au Electrode Surface Probed by Time-Resolved Vibrational Sum Frequency Generation Spectroscopy. *J. Phys. Chem. C* **2012**, *116*, 26377–26384.
- (56) Ricks, A. M.; Anfuso, C. L.; Rodríguez-Córdoba, W.; Lian, T. Vibrational Relaxation Dynamics of Catalysts on TiO₂ Rutile (110) Single Crystal Surfaces and Anatase Nanoporous Thin Films. *Chem. Phys.* **2013**, *422*, 264–271.
- (57) Calabrese, C.; Vanselow, H.; Petersen, P. B. Deconstructing the Heterogeneity of Surface-Bound Catalysts: Rutile Surface Structure Affects Molecular Properties. *J. Phys. Chem. C* **2016**, *120*, 1515–1522.
- (58) Ge, A.; Rudshiteyn, B.; Zhu, J.; Maurer, R. J.; Batista, V. S.; Lian, T. Electron-Hole-Pair-Induced Vibrational Energy Relaxation of Rhenium Catalysts on Gold Surfaces. *J. Phys. Chem. Lett.* **2018**, *9*, 406–412.
- (59) Hamm, P.; Zanni, M. *Concepts and Methods of 2d Infrared Spectroscopy*; Cambridge University Press, 2011.
- (60) Fayer, M. D. *Ultrafast Infrared Vibrational Spectroscopy*; CRC Press, 2013; Vol. 2, p 487.
- (61) Kraack, J. P.; Hamm, P. Surface-Sensitive and Surface-Specific Ultrafast Two-Dimensional Vibrational Spectroscopy. *Chem. Rev.* **2017**, *117*, 10623–10664.
- (62) Kraack, J. P.; Lotti, D.; Hamm, P. Ultrafast, Multidimensional Attenuated Total Reflectance Spectroscopy of Adsorbates at Metal Surfaces. *J. Phys. Chem. Lett.* **2014**, *5*, 2325–2329.
- (63) Kraack, J. P.; Lotti, D.; Hamm, P. *Surface-Enhanced, Multi-Dimensional Attenuated Total Reflectance Spectroscopy*; SPIE Nano-science + Engineering, SPIE, 2015; p 9.
- (64) Kraack, J. P.; Frei, A.; Alberto, R.; Hamm, P. Ultrafast Vibrational Energy Transfer in Catalytic Monolayers at Solid-Liquid Interfaces. *J. Phys. Chem. Lett.* **2017**, *8*, 2489–2495.
- (65) Kraack, J. P.; Sévery, L.; Tilley, S. D.; Hamm, P. Plasmonic Substrates Do Not Promote Vibrational Energy Transfer at Solid-Liquid Interfaces. *J. Phys. Chem. Lett.* **2018**, *9*, 49–56.

- (66) Kraack, J. P.; Hamm, P. Surface-Sensitive and Surface-Specific Ultrafast Two-Dimensional Vibrational Spectroscopy. *Chem. Rev.* **2016**, *117*, 10623.
- (67) Rosenfeld, D. E.; Gengeliczki, Z.; Smith, B. J.; Stack, T. D. P.; Fayer, M. D. Structural Dynamics of a Catalytic Monolayer Probed by Ultrafast 2d Ir Vibrational Echoes. *Science* **2011**, *334*, 634–639.
- (68) Oudenhoven, T. A.; Joo, Y.; Laaser, J. E.; Gopalan, P.; Zanni, M. T. Dye Aggregation Identified by Vibrational Coupling Using 2d Ir Spectroscopy. *J. Chem. Phys.* **2015**, *142*, 212449.
- (69) Yan, C.; Yuan, R.; Pfalzgraff, W. C.; Nishida, J.; Wang, L.; Markland, T. E.; Fayer, M. D. Unraveling the Dynamics and Structure of Functionalized Self-Assembled Monolayers on Gold Using 2d Ir Spectroscopy and Md Simulations. *Proc. Natl. Acad. Sci. U.S.A.* **2016**, *113*, 4929–4934.
- (70) Xiong, W.; Laaser, J. E.; Mehlenbacher, R. D.; Zanni, M. T. Adding a Dimension to the Infrared Spectra of Interfaces Using Heterodyne Detected 2d Sum-Frequency Generation (Hd 2d SFG) Spectroscopy. *Proc. Natl. Acad. Sci. U.S.A.* **2011**, *108*, 20902–20907.
- (71) Laaser, J. E.; Zanni, M. T. Extracting Structural Information from the Polarization Dependence of One- and Two-Dimensional Sum Frequency Generation Spectra. *J. Phys. Chem. A* **2013**, *117*, 5875–5890.
- (72) Wang, J.; Clark, M. L.; Li, Y.; Kaslan, C. L.; Kubiak, C. P.; Xiong, W. Short-Range Catalyst–Surface Interactions Revealed by Heterodyne Two-Dimensional Sum Frequency Generation Spectroscopy. *J. Phys. Chem. Lett.* **2015**, *6*, 4204–4209.
- (73) Vanselous, H.; Stingel, A. M.; Petersen, P. B. Interferometric 2d Sum Frequency Generation Spectroscopy Reveals Structural Heterogeneity of Catalytic Monolayers on Transparent Materials. *J. Phys. Chem. Lett.* **2017**, *8*, 825–830.
- (74) Vanselous, H.; Petersen, P. B. Extending the Capabilities of Heterodyne-Detected Sum-Frequency Generation Spectroscopy: Probing Any Interface in Any Polarization Combination. *J. Phys. Chem. C* **2016**, *120*, 8175–8184.
- (75) Calabrese, C.; Vanselous, H.; Petersen, P. B. Deconstructing the Heterogeneity of Surface-Bound Catalysts: Rutile Surface Structure Affects Molecular Properties. *J. Phys. Chem. C* **2016**, *120*, 1515–1522.
- (76) Skibinski, E. S.; Song, A.; DeBenedetti, W. J. I.; Ortoll-Bloch, A. G.; Hines, M. A. Solution Deposition of Self-Assembled Benzoate Monolayers on Rutile (110): Effect of Π – Π Interactions on Monolayer Structure. *J. Phys. Chem. C* **2016**, *120*, 11581–11589.
- (77) Ghosh, A.; Smits, M.; Bredenbeck, J.; Dijkhuizen, N.; Bonn, M. Femtosecond Time-Resolved and Two-Dimensional Vibrational Sum Frequency Spectroscopic Instrumentation to Study Structural Dynamics at Interfaces. *Rev. Sci. Instrum.* **2008**, *79*, 093907.
- (78) Anfuso, C. L.; Xiao, D.; Ricks, A. M.; Negre, C. F. A.; Batista, V. S.; Lian, T. Orientation of a Series of CO₂ Reduction Catalysts on Single Crystal TiO₂ Probed by Phase-Sensitive Vibrational Sum Frequency Generation Spectroscopy (Ps-Vsfg). *J. Phys. Chem. C* **2012**, *116*, 24107–24114.
- (79) Frisch, M. J.; Trucks, G. W.; Schlegel, H. B.; Scuseria, G. E.; Robb, M. A.; Cheeseman, J. R.; Scalmani, G.; Barone, V.; Petersson, G. A.; Nakatsuji, H.; Caricato, M.; Li, X.; Hratchian, H. P.; Izmaylov, A. F.; Bloino, J.; Zheng, G.; Sonnenberg, J. L.; Hada, M.; Ehara, M.; Toyota, K.; Fukuda, R.; Hasegawa, J.; Ishida, M.; Nakajima, T.; Honda, Y.; Kitao, O.; Nakai, H.; Vreven, T.; Montgomery, J. A., Jr.; Peralta, J. E.; Ogliaro, Ö.; Foresman, J. B.; Ortiz, J. V.; Cioslowski, J.; Fox, D. J. *Gaussian 09*, Revision D.01; Wallingford CT, 2016.
- (80) Becke, A. D. Density-Functional Thermochemistry.Iii. The Role of Exact Exchange. *J. Chem. Phys.* **1993**, *98*, 5648–5652.
- (81) Andrae, D.; Häußermann, U.; Dolg, M.; Stoll, H.; Preuß, H. Energy-Adjusted *Ab Initio* Pseudopotentials for the Second and Third Row Transition Elements. *Theor. Chim. Acta* **1990**, *77*, 123–141.
- (82) Hay, P. J.; Wadt, W. R. *Ab Initio* Effective Core Potentials for Molecular Calculations. Potentials for the Transition Metal Atoms Sc to Hg. *J. Chem. Phys.* **1985**, *82*, 270–283.
- (83) Stevens, W. J.; Krauss, M.; Basch, H.; Jasien, P. G. Relativistic Compact Effective Potentials and Efficient, Shared-Exponent Basis Sets for the Third-, Fourth-, and Fifth-Row Atoms. *Can. J. Chem.* **1992**, *70*, 612–630.
- (84) Yan, E. C. Y.; Fu, L.; Wang, Z.; Liu, W. Biological Macromolecules at Interfaces Probed by Chiral Vibrational Sum Frequency Generation Spectroscopy. *Chem. Rev.* **2014**, *114*, 8471–8498.
- (85) Wang, H.-F.; Gan, W.; Lu, R.; Rao, Y.; Wu, B.-H. Quantitative Spectral and Orientational Analysis in Surface Sum Frequency Generation Vibrational Spectroscopy (SFG-Vs). *Int. Rev. Phys. Chem.* **2005**, *24*, 191–256.
- (86) Zhuang, X.; Miranda, P. B.; Kim, D.; Shen, Y. R. Mapping Molecular Orientation and Conformation at Interfaces by Surface Nonlinear Optics. *Phys. Rev. B: Condens. Matter Mater. Phys.* **1999**, *59*, 12632–12640.
- (87) Rams, J.; Tejeda, A.; Cabrera, J. M. Refractive Indices of Rutile as a Function of Temperature and Wavelength. *J. Appl. Phys.* **1997**, *82*, 994–997.
- (88) DeVore, J. R. Refractive Indices of Rutile and Sphalerite. *J. Opt. Soc. Am.* **1951**, *41*, 416–419.
- (89) Barone, V. Vibrational Zero-Point Energies and Thermodynamic Functions Beyond the Harmonic Approximation. *J. Chem. Phys.* **2004**, *120*, 3059–3065.
- (90) Barone, V. Anharmonic Vibrational Properties by a Fully Automated Second-Order Perturbative Approach. *J. Chem. Phys.* **2005**, *122*, 014108.
- (91) Xiong, W.; Laaser, J. E.; Paoprasert, P.; Franking, R. A.; Hamers, R. J.; Gopalan, P.; Zanni, M. T. Transient 2d Ir Spectroscopy of Charge Injection in Dye-Sensitized Nanocrystalline Thin Films. *J. Am. Chem. Soc.* **2009**, *131*, 18040–18041.
- (92) Laaser, J. E.; Christianson, J. R.; Oudenhoven, T. A.; Joo, Y.; Gopalan, P.; Schmidt, J. R.; Zanni, M. T. Dye Self-Association Identified by Intermolecular Couplings between Vibrational Modes as Revealed by Infrared Spectroscopy, and Implications for Electron Injection. *J. Phys. Chem. C* **2014**, *118*, 5854–5861.
- (93) Shen, Y. R. *The Principles of Nonlinear Optics*; Wiley-Interscience: New York, 1984.
- (94) Shen, Y. R. Phase-Sensitive Sum-Frequency Spectroscopy. *Annu. Rev. Phys. Chem.* **2013**, *64*, 129–150.
- (95) Nihonyanagi, S.; Mondal, J. A.; Yamaguchi, S.; Tahara, T. Structure and Dynamics of Interfacial Water Studied by Heterodyne-Detected Vibrational Sum-Frequency Generation. *Annu. Rev. Phys. Chem.* **2013**, *64*, 579–603.
- (96) Li, Z.; Wang, J.; Li, Y.; Xiong, W. Solving the “Magic Angle” Challenge in Determining Molecular Orientation Heterogeneity at Interfaces. *J. Phys. Chem. C* **2016**, *120*, 20239–20246.
- (97) Hsieh, C.-S.; Okuno, M.; Hunger, J.; Backus, E. H. G.; Nagata, Y.; Bonn, M. Aqueous Heterogeneity at the Air/Water Interface Revealed by 2d-Hd-SFG Spectroscopy. *Angew. Chem., Int. Ed.* **2014**, *53*, 8146–8149.
- (98) Inoue, K.-i.; Nihonyanagi, S.; Singh, P. C.; Yamaguchi, S.; Tahara, T. 2d Heterodyne-Detected Sum Frequency Generation Study on the Ultrafast Vibrational Dynamics of H₂O and H₂D Water at Charged Interfaces. *J. Chem. Phys.* **2015**, *142*, 212431.
- (99) Cervetto, V.; Helbing, J.; Bredenbeck, J.; Hamm, P. Double-Resonance Versus Pulsed Fourier Transform Two-Dimensional Infrared Spectroscopy: An Experimental and Theoretical Comparison. *J. Chem. Phys.* **2004**, *121*, 5935–5942.
- (100) Shim, S.-H.; Strasfeld, D. B.; Ling, Y. L.; Zanni, M. T. Automated 2d Ir Spectroscopy Using a Mid-Ir Pulse Shaper and Application of This Technology to the Human Islet Amyloid Polypeptide. *Proc. Natl. Acad. Sci. U. S. A.* **2007**, *104*, 14197–14202.
- (101) Shim, S.-H.; Zanni, M. T. How to Turn Your Pump-Probe Instrument into a Multidimensional Spectrometer: 2d Ir and Vis Spectroscopies Via Pulse Shaping. *Phys. Chem. Chem. Phys.* **2009**, *11*, 748–761.
- (102) Ghosh, A.; Ho, J.-J.; Serrano, A. L.; Skoff, D. R.; Zhang, T.; Zanni, M. T. Two-Dimensional Sum-Frequency Generation (2d SFG) Spectroscopy: Summary of Principles and Its Application to Amyloid Fiber Monolayers. *Faraday Discuss.* **2015**, *177*, 493–505.

(103) Ho, J.-J.; Skoff, D. R.; Ghosh, A.; Zanni, M. T. Structural Characterization of Single-Stranded DNA Monolayers Using Two-Dimensional Sum Frequency Generation Spectroscopy. *J. Phys. Chem. B* **2015**, *119*, 10586–10596.